Eur. Phys. J. B **22**, 257–265 (2001)

THE EUROPEAN PHYSICAL JOURNAL B
EDP Sciences

Optical absorption and energy-loss spectra of aligned carbon nanotubes

F.J. García-Vidal[1] and J.M. Pitarke[2,a]

[1] Departamento de Física Teórica de la Materia Condensada, Facultad de Ciencias, Universidad Autónoma de Madrid, 28049 Madrid, Spain
[2] Materia Kondentsatuaren Fisika Saila, Zientzi Fakultatea, Euskal Herriko Unibertsitatea, 644 Posta kutxatila, 48080 Bilbo, Basque Country, Spain
and
Donostia International Physics Center (DIPC) and Centro Mixto CSIC-UPV/EHU, Donostia, Basque Country, Spain

Received 18 January 2001

Abstract. Optical-absorption cross-sections and energy-loss spectra of aligned multishell carbon nanotubes are investigated, on the basis of photonic band-structure calculations. A local graphite-like dielectric tensor is assigned to every point of the tubules, and the effective transverse dielectric function of the composite is computed by solving Maxwell's equations in media with tensor-like dielectric functions. A Maxwell-Garnett-like approach appropriate to the case of infinitely long anisotropic tubules is also developed. Our full calculations indicate that the experimentally measured macroscopic dielectric function of carbon nanotube materials is the result of a strong electromagnetic coupling between the tubes. An analysis of the electric-field pattern associated with this coupling is presented, showing that in the close-packed regime the incident radiation excites a very localized tangential surface plasmon.

PACS. 78.66.Sq Composite materials – 41.20.Jb Electromagnetic wave propagation; radiowave propagation – 61.46.+w Nanoscale materials: clusters, nanoparticles, nanotubes, and nanocrystals

1 Introduction

The description of the electronic response of carbon nanotubes [1,2] has been a challenge for theoretical and experimental investigations. Various theoretical studies of plasmon excitations in single-shell carbon nanotubes were reported [3–5], electron-energy-loss spectra from individual multishell nanotubes were investigated [6–9] by changing the number of shells, and curvature was found to induce little effect on the covalent bonding of multishell nanotubes [10]. With the availability of aligned carbon nanotube films [11,12], optical measurements were carried out with polarized light [12,13], thereby evaluating the frequency-dependent effective dielectric function of the composite and showing that carbon nanotubes have an intrinsic and anisotropic metallic behaviour. Accurate calculations of the effective dielectric function of densely packed carbon nanotubes, as obtained by solving Maxwell's equations with the use of tensor-like dielectric functions, have been carried out only very recently [14,15].

In this paper we report extensive calculations of the frequency-dependent effective dielectric function of a composite made up of aligned carbon nanotubes embedded in an otherwise homogeneous medium. In Section 2 our effective medium theory is described. We take an electromagnetic wave normally incident on the structure, and focus on the case of electromagnetic waves polarized normal to the cylinders (p polarization). For this polarization we also introduce a generalized Maxwell-Garnett (MG) [16] effective dielectric function appropriate for anisotropic tubules. Absorption of p polarized light is found to be sensitive to both the inner cavity of hollow tubules and the anisotropy, which we first investigate in Section 3.1 within the MG approach. In Section 3.2 we focus on the close-packed regime, showing that the experimentally measured macroscopic dielectric function of aligned carbon nanotubes is the result of a strong electromagnetic coupling between the tubes. Calculations of the electric field, the induced charge, and the so-called energy-loss function, *i.e.*, the imaginary part of the effective inverse dielectric function, are also presented, for various values of the filling fraction and the ratio of the internal and external radii of the cylinders. The main conclusions of our work are addressed in Section 4.

2 Theory

Take a periodic array of infinitely long multishell nanotubes of inner and outer radii r and R, respectively, arranged in a square array with lattice constant $a = 2\,x\,R$,

[a] e-mail: wmppitoj@lg.ehu.es

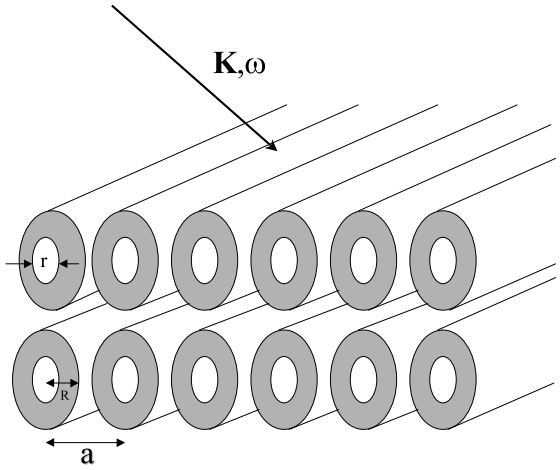

Fig. 1. Multishell nanotubes of inner and outer radii r and R, respectively, arranged in a square array with lattice constant a. The cylinders are infinitely long in the y-direction. The electromagnetic interaction of this structure with a normally incident plane wave of momentum $\mathbf{k}$ [$k_y = k_z = 0$] and energy ω is investigated.

as shown in Figure 1. These tubules are assumed to be embedded in an insulating medium, with a real and positive dielectric constant ε_0. In the energy range of interest in the interpretation of absorption cross sections and energy-loss spectra the diameter of typical multishell carbon nanotubes ($2\,R \sim 10$ nm) is small in comparison to the wavelength of light, and we also assume that this diameter is large enough that a macroscopic dielectric function is ascribable to the tubules. For simplicity, the magnetic permeabilities will be assumed to be equal to unity in all media.

Planar graphite is a highly anisotropic material, and the dielectric function is a tensor. This tensor may be diagonalized, by choosing Cartesian coordinates with two of the axes lying in the basal plane and the third axis being the so-called c-axis. One defines the dielectric function $\varepsilon_\perp(\omega)$ perpendicular to the c-axis and the dielectric function $\varepsilon_\parallel(\omega)$ for the electric field parallel to the c-axis. For carbon nanotubes, we assume full transferability of the dielectric tensor of planar graphite to the curved geometry of carbon tubules, as suggested by Lucas *et al.* [17] for the case of multishell fullerenes. Hence, we simply assign a local graphite-like dielectric tensor to every point inside the nanotube and outside the inner core, and write

$$\hat{\varepsilon}(\omega) = \varepsilon_\perp(\omega)(\boldsymbol{\theta\theta} + \mathbf{zz}) + \varepsilon_\parallel(\omega)\mathbf{rr}, \tag{1}$$

where $\boldsymbol{\theta\theta}$, $\mathbf{zz}$, and $\mathbf{rr}$ are the unitary basis vectors of cylindrical coordinates.

In the long-wavelength limit, a composite material may be treated as if it were homogeneous, with the use of an effective dielectric function ε_{eff}. The optical absorption cross section of the composite is then directly given by $\operatorname{Im}\varepsilon_{\text{eff}}(\omega)$. Also, for small values of the dimensionless parameter qR ($qR < 1$), q being the momentum transfer, the energy-loss spectra of a broad beam of swift electrons penetrating the composite is found [18,19] to be well described by the $q \to 0$ limit of the imaginary part of the effective dielectric function, *i.e.*, the so-called energy-loss function, $\operatorname{Im}[-\varepsilon_{\text{eff}}^{-1}(\omega)]$.

We consider an electromagnetic wave normally incident on the structure, so that $k_y = k_z = 0$. For this propagation direction there are two different values of $\varepsilon_{\text{eff}}(\omega)$ corresponding to s and p polarizations. In the case of s polarization the electric field is parallel to the cylinders at every point, and is not modified by the presence of the interfaces. Hence, the s effective dielectric function of the composite is simply the weighted average of the dielectric functions of the constituents [20].

For electromagnetic waves polarized normal to the cylinders (p polarization), the electric field may be strongly modified by the presence of the interfaces. An elementary analysis shows that

$$(\varepsilon_{\text{eff}} - \varepsilon_0)\mathbf{E} = f(\hat{\varepsilon} - \hat{\varepsilon}_0)\mathbf{E}_{\text{in}}, \tag{2}$$

where $\mathbf{E}$ is the average electric field over the composite,

$$\mathbf{E} = f\mathbf{E}_{\text{in}} + (1-f)\mathbf{E}_{\text{out}}, \tag{3}$$

$\mathbf{E}_{\text{in}}$ and $\mathbf{E}_{\text{out}}$ representing the average electric field inside and outside the tubules, respectively, both lying in the plane of periodicity.

In the case of a single two-dimensional circular inclusion (plain or hollow cylinder) embedded in an otherwise homogeneous medium ($f \to 0$), one easily finds

$$(\hat{\varepsilon} - \hat{\varepsilon}_0)\mathbf{E}_{\text{in}} = \varepsilon_0\alpha\mathbf{E}, \tag{4}$$

and equation (2) then yields

$$\varepsilon_{\text{eff}} = \varepsilon_0\,(1 + f\,\alpha)\,, \tag{5}$$

where α represents the in-plane dipole polarizability per unit volume.

As long as the composite is made of a sparse ($f \ll 1$) distribution of cylinders the presence of multipolar modes can be neglected [21], and the interaction between the cylinders can be introduced by simply replacing the average electric field $\mathbf{E}$ in equation (4) by $\mathbf{E}_{\text{out}}$. Then, with the aid of equations (2) and (3), one finds

$$\varepsilon_{\text{eff}} = \varepsilon_0\left(1 + f\,\frac{\alpha}{1 - f\,L\,\alpha}\right) \tag{6}$$

and

$$\varepsilon_{\text{eff}}^{-1} = \varepsilon_0^{-1}\left(1 - f\,\frac{\alpha}{1 + f\,L\,\alpha}\right), \tag{7}$$

with the geometrical factor $L = 1/2$. For cylindrical geometry [22],

$$\alpha = \frac{2}{(1-\rho^2)} \times \frac{(\varepsilon_\parallel\Delta - \varepsilon_0)(\varepsilon_\parallel\Delta + \varepsilon_0) - (\varepsilon_\parallel\Delta - \varepsilon_0)(\varepsilon_\parallel\Delta + \varepsilon_0)\rho^{2\Delta}}{(\varepsilon_\parallel\Delta + \varepsilon_0)(\varepsilon_\parallel\Delta + \varepsilon_0) - (\varepsilon_\parallel\Delta - \varepsilon_0)(\varepsilon_\parallel\Delta - \varepsilon_0)\rho^{2\Delta}}, \tag{8}$$

where

$$\Delta = \sqrt{\varepsilon_\perp/\varepsilon_\parallel}. \tag{9}$$

Equation (8) with $\rho = 0$ and $\varepsilon_\parallel(\omega) = \varepsilon_\perp(\omega)$ reduces to the well-known polarizability per unit volume of a plain isotropic cylinder.

Equation (6) is a generalization, appropriate for anisotropic tubules, of the well-known MG effective dielectric function derived by Maxwell-Garnett for a system of spherical particles [16].

In the non-sparse or packed regime, where the presence of multipolar modes cannot be neglected, the inclusion of the full electromagnetic interaction between the tubules is unavoidable. In order to compute, with full inclusion of this interaction, the effective dielectric function of our periodic system, we have followed the method developed in references [23] and [24] for the calculation of dispersion relationships $k(\omega)$ of Bloch waves in structured materials with tensor-like dielectric functions.

In the long-wavelength limit the composite material supports, for each polarization, only two degenerate electromagnetic Bloch waves with vectors k and $-k$ for which $k(\omega)$ roughly follows the dispersion relation of free light. Hence, in this limit the composite may be treated as if it were homogeneous, with an effective transverse dielectric function

$$\varepsilon_{\rm eff}(\omega) = \frac{k^2(\omega)c^2}{\omega^2}, \tag{10}$$

where c represents the speed of light.

3 Results and discussion

We consider a periodic array of hollow multishell carbon nanotubes (see Fig. 1) with $\varepsilon_0 = 1$, and take the principal dielectric functions $\varepsilon_\perp(\omega)$ and $\varepsilon_\parallel(\omega)$ of graphite from reference [25]. The real and imaginary parts of these components, as well as their corresponding energy-loss functions, are represented in Figure 2 for energies up to 8 eV. In this energy range, optical transitions mainly involve the π bands arising from the atomic $2p_z$ orbitals. The peak in $\mathrm{Im}\,\varepsilon_\perp(\omega)$ at ~ 4.6 eV is associated with the maximum in the joint density of states of the π valence and conduction bands. The so-called π plasmon at ~ 7 eV, where $\mathrm{Re}\,\varepsilon_\perp(\omega)$ and $\mathrm{Im}\,\varepsilon_\perp(\omega)$ are small, is due to a $\pi - \pi^*$ interband transition [26].

For energies over ~ 5 eV, the principal dielectric function $\varepsilon_\perp(\omega)$ is close to that of a free-electron gas. Thus, for these energies π electrons within each shell act as if they were free. However, for free-electron-like materials $\mathrm{Re}\,\varepsilon_\perp(\omega)$ approaches large negative values with decreasing energy, whereas for graphite the plasmon region with $\mathrm{Re}\,\varepsilon_\perp(\omega)$ negative is bounded from below and from above at about 5 and 7 eV.

Calculations of the s component of the effective dielectric function of an array of coaxial nanotubes were reported in reference [15] for various values of the filling fraction f of the tubes, showing that they roughly reproduce the experimentally determined $\mathrm{Im}\epsilon_{\rm eff}(\omega)$ for $f \sim 0.5$.

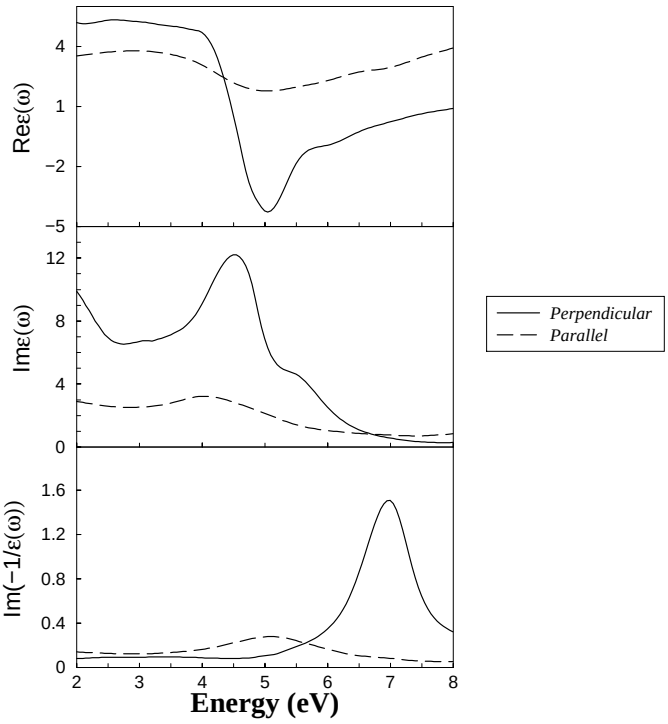

Fig. 2. Energy dependence of the real and imaginary parts of the principal dielectric functions, $\mathrm{Re}\,\varepsilon(\omega)$ and $\mathrm{Im}\,\varepsilon(\omega)$, and the energy-loss function, $\mathrm{Im}[-\varepsilon^{-1}(\omega)]$, for graphite, taken from reference [25]. Solid and dashed lines represent components perpendicular and parallel to the c-axis, respectively.

Here we focus on the case of electromagnetic waves polarized normal to the cylinders (p polarization), which we first investigate within the MG approach.

3.1 Maxwell-Garnett approach

First of all, we ignore the anisotropy and simply assume that $\varepsilon(\omega) = \varepsilon_\parallel(\omega) = \varepsilon_\perp(\omega)$. In this case, the in-plane dipole polarizability of equation (8) can be expressed in the form of a spectral representation:

$$\alpha = -\left(\frac{B_+}{u - m_-} + \frac{B_-}{u - m_+}\right), \tag{11}$$

where u is the spectral variable

$$u = (1 - \varepsilon/\varepsilon_0)^{-1}, \tag{12}$$

$m_\pm$ are depolarization factors,

$$m_\pm = \frac{1}{2}(1 \pm \rho), \tag{13}$$

and $B\pm$ are the strengths of the corresponding normal modes,

$$B_\pm = \frac{1}{2}. \tag{14}$$

The depolarization factors of equation (13) lie on the segment [0,1] for all values of ρ. Hence, normal modes

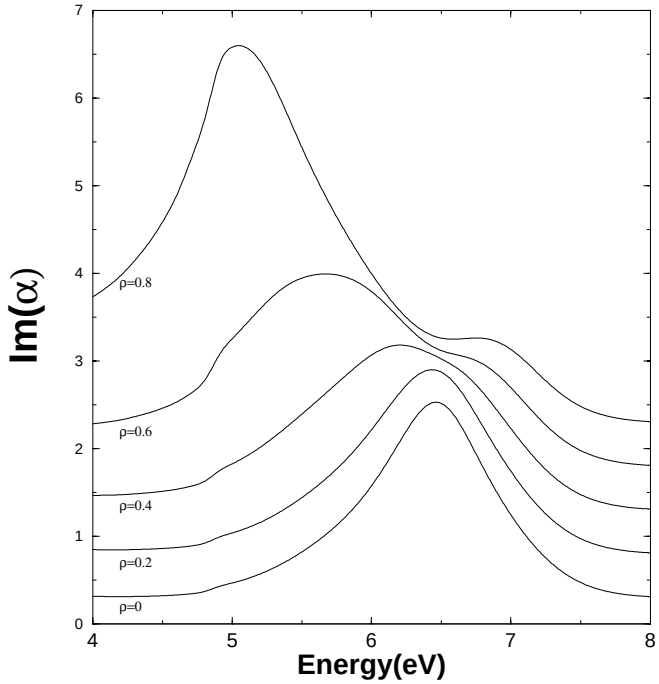

Fig. 3. Imaginary part of the in-plane dipole polarizability per unit volume of isotropic plain ($\rho = 0$) and hollow ($\rho \neq 0$) cylinders, as obtained either from equation (8) with $\varepsilon_{\parallel}(\omega) = \varepsilon_{\perp}(\omega)$ or from equation (11), as a function of frequency ω and for various values of the ratio between the inner and outer radii of the cylinders: $\rho = 0, 0.2, 0.4, 0.6$, and 0.8.

only occur in the so-called plasmon region where the dielectric function $\varepsilon(\omega)$ is negative or equal to zero. For graphite, this plasmon region is bounded from below and from above at about 5 and 7 eV where the spectral variable u is never smaller than $u \sim 0.2$. As the ratio between the inner and outer radii of the tubes goes to unity ($\rho \to 1$), one easily finds

$$\alpha = \frac{1}{2}\left(\varepsilon - \varepsilon^{-1}\right). \tag{15}$$

In the case of an isolated plain ($\rho = 0$) or hollow ($\rho \neq 0$) cylinder, both $\mathrm{Im}\,\varepsilon_{\mathrm{eff}}(\omega)$ and $\mathrm{Im}[-\varepsilon_{\mathrm{eff}}^{-1}(\omega)]$ are proportional to the imaginary part of the in-plane dipole polarizability α, and satisfy the relation

$$\mathrm{Im}\left[-\varepsilon_{\mathrm{eff}}^{-1}\right] = \epsilon_0^{-2}\,\mathrm{Im}\,\varepsilon_{\mathrm{eff}}. \tag{16}$$

Hence, the absorption and energy-loss spectra of isolated plain ($\rho = 0$) cylinders in vacuum ($\varepsilon_0 = 1$) exhibit a strong maximum at ~ 6.5 eV where $u = 1/2$ and $\varepsilon(\omega) = -1$, as shown in Figure 3. For hollow tubes ($\rho \neq 0$), there are two distinct dipolar modes with either tangential or radial symmetry, at $u = m_- < 1/2$ and $u = m_+ > 1/2$, respectively, similar to those present in the case of a thin planar film [27] and a spherical shell [28]. The corresponding peak heights in $\mathrm{Im}\,\alpha(\omega)$ are easily found to be $H\,B_{\pm}/\sqrt{m_{\pm}}$, H representing the peak height in the bulk energy-loss function, $\mathrm{Im}[-\varepsilon^{-1}(\omega)]$. Thus, the tangential mode at $u = (1-\rho)/2$ appears to be more pronounced than the radial mode at $u = (1+\rho)/2$ (see Fig. 3). For $\rho = 0.2$ these modes are not resolved, due to the smoothing effect of the large damping associated with non-negligible values of $\mathrm{Im}\,\varepsilon_{\perp}(\omega)$, and the effect of the empty core is simply to redshift and soften this combined plasmon mode. For values of ρ in the range $0.2 < \rho < 0.8$ the tangential and radial plasmons are clearly identified. However, for larger values of ρ the tangential resonance condition ($u \to 0$) is never satisfied. Furthermore, in the limit as $\rho \to 1$ the effective dielectric function is given by equation (15), thus showing the radial plasmon resonance at ~ 7 eV, where $u = 1$ and $\varepsilon(\omega) = 0$, and the characteristic peak at ~ 4.6 eV associated with the maximum in $\mathrm{Im}\,\varepsilon(\omega)$.

Still ignoring the anisotropy, the MG effective dielectric function and inverse dielectric function of equations (6) and (7) can also be expressed in the form of a spectral representation:

$$\varepsilon_{\mathrm{eff}} = \varepsilon_0\left[1 - f\left(\frac{B_+}{u - m_-} + \frac{B_-}{u - m_+}\right)\right] \tag{17}$$

and

$$\varepsilon_{\mathrm{eff}}^{-1} = \varepsilon_0\left[1 + f\left(\frac{B_-}{u - n_-} + \frac{B_+}{u - n_+}\right)\right], \tag{18}$$

where

$$m_{\pm} = \frac{1}{2}\left(1 - \frac{1}{2}f \pm \frac{1}{2}\sqrt{f^2 + 4\rho^2}\right), \tag{19}$$

$$n_{\pm} = \frac{1}{2}\left(1 + \frac{1}{2}f \pm \frac{1}{2}\sqrt{f^2 + 4\rho^2}\right), \tag{20}$$

and

$$B_{\pm} = \frac{1}{2}\,\frac{\sqrt{f^2 + 4\rho^2} \pm f}{\sqrt{f^2 + 4\rho^2}}, \tag{21}$$

the mode strengths ($B_- \leq 1/2$ and $B_+ \geq 1/2$) adding up to unity, *i.e.*, $B_+ + B_- = 1$. Also, $m_-, n_- \leq 1/2$ and $m_+, n_+ \geq 1/2$.

In Figure 4, we show the surface-mode positions $m_{\pm}$ and $n_{\pm}$ of equations (19) and (20), as a function of ρ, for various values of the ratio x between the lattice constant and the outer diameter of the cylinders. In the dilute limit ($x \to \infty$), both $m_{\pm}$ and $n_{\pm}$ coincide with the depolarization factors of equation (13) entering the spectral representation of the polarizability. As x decreases, for each value of ρ these surface modes split into four distinct modes, $m_{\pm}$ and $n_{\pm}$, which satisfy the simple relation:

$$n_{\pm} = 1 - m_{\mp}. \tag{22}$$

The strengths $B_{\pm}$, as obtained from equation (21), are plotted in Figure 5, as a function of ρ, also for various values of the ratio x between the lattice constant and the outer diameter of the cylinders. As in the case of the depolarization factors, in the dilute limit ($x \to \infty$) the strengths $B_{\pm}$ coincide with the strengths $B_{\pm} = 1/2$ entering the spectral representation of the polarizability. As x decreases, these strengths are different, especially

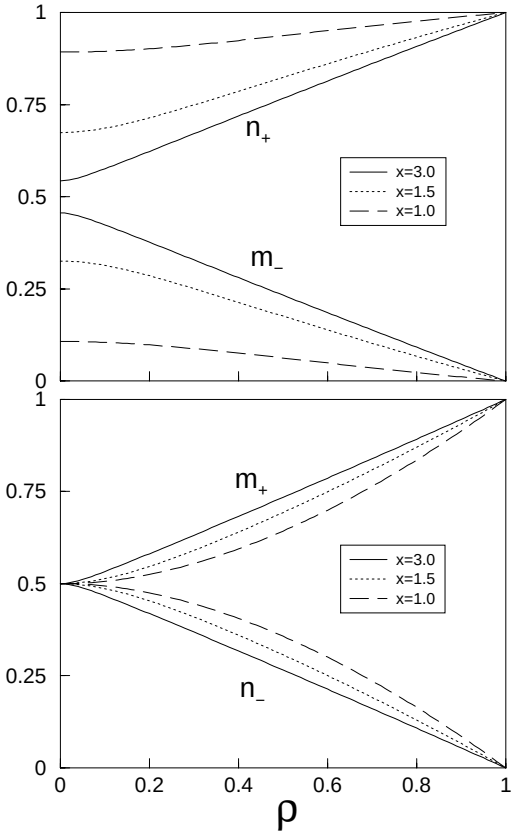

Fig. 4. Surface-mode positions: (a) m_-, n_+ and (b) m_+, n_-, as obtained from equations (19) and (20) *versus* ρ, for various values of the ratio between the lattice constant and the outer diameter of the cylinders: $x = 3$ (solid lines), $x = 1.5$ (dotted lines), and $x = 1$ (dashed lines).

for small values of ρ, showing that the strongest modes occur at $u = m_-$ and $u = n_+$ with the depolarization factors m_- and n_+ lying on the segments $[0, (1-f)/2]$ (low-energy resonance) and $[(1+f)/2, 1]$ (high-energy resonance), respectively (see Fig. 4). The modes at $u = m_-$ and $u = n_+$, which have no strength for $\rho = 0$, lie on the segments [1/2,1] and [0,1/2], respectively. For $x \to 1$, one easily finds $B_+ = 1/(1+\rho^2)$ and $B_- = \rho^2/(1+\rho^2)$, thereby showing that modes occurring at $u = m_-$ and $u = n_+$ dominate. Hence, when cylinders are touching and for most values of ρ there is a single dominating resonance condition at $u \to 0$ (low energy) and $u \to 1$ (high energy) in $\mathrm{Im}\,\varepsilon_{\mathrm{eff}}(\omega)$ and $\mathrm{Im}[-\varepsilon_{\mathrm{eff}}^{-1}(\omega)]$, respectively, the strength of the remaining resonance being negligible.

From equations (17) and (18), we have calculated $\mathrm{Im}\,\varepsilon_{\mathrm{eff}}(\omega)/f$ and $\mathrm{Im}[-\varepsilon_{\mathrm{eff}}^{-1}(\omega)]/f$ for various values of x and the ratio ρ between the inner and outer radii of the cylinders. While for $x = 3$ both $\mathrm{Im}\,\varepsilon_{\mathrm{eff}}(\omega)/f$ and $\mathrm{Im}[-\varepsilon_{\mathrm{eff}}^{-1}(\omega)]/f$ are found to nearly coincide with the imaginary part of the polarizability of equation (11) (see Fig. 3), we have found that the trend with decreasing the distance between the cylinders is for the low-energy and high-energy resonances to slightly move from the single-cylinder dipole resonances at $u = (1 \pm \rho)/2$ to lower and higher energies, respectively; this is obvious in Figure 6, where $\mathrm{Im}\,\varepsilon_{\mathrm{eff}}(\omega)/f$ and $\mathrm{Im}[-\varepsilon_{\mathrm{eff}}^{-1}(\omega)]/f$, as obtained from

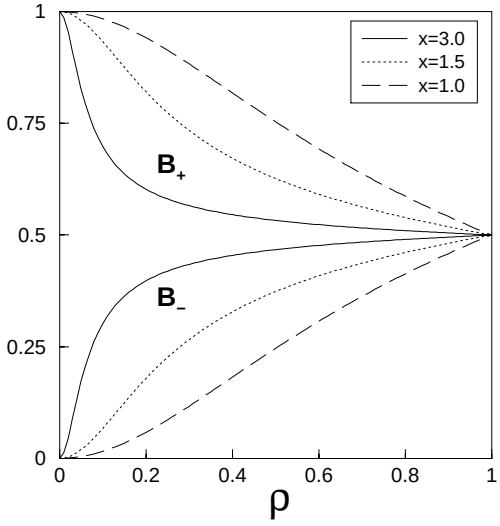

Fig. 5. Strengths $B_\pm$, as obtained from equation (21) *versus* ρ, for various values of the ratio between the lattice constant and the outer diameter of the cylinders: $x = 3$ (solid lines), $x = 1.5$ (dotted lines), and $x = 1$ (dashed lines).

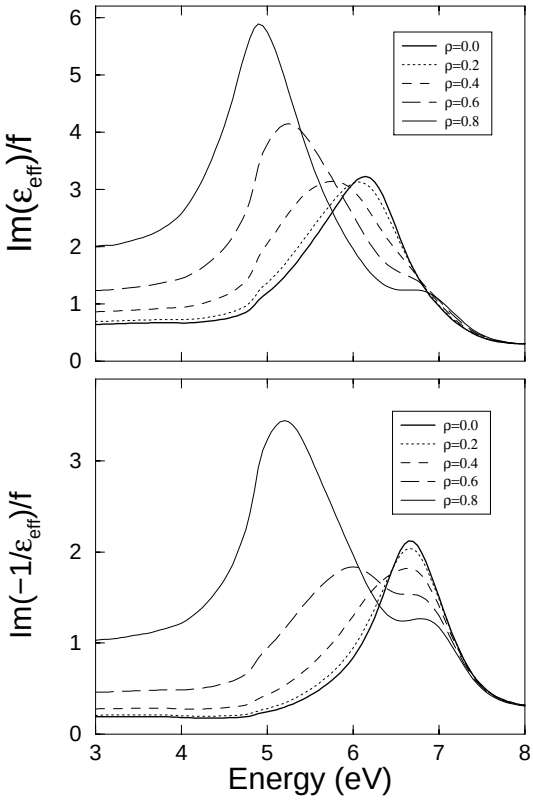

Fig. 6. Imaginary part of the MG effective dielectric function and MG effective energy-loss function of the periodic system described in Figure 1, as obtained from either equations (6) and (7) with $\varepsilon_\parallel(\omega) = \varepsilon_\perp(\omega)$ or from equations (17) and (18), and for various values of the ratio between the inner and outer radii of the cylinders: $\rho = 0$ (solid line), $\rho = 0.2$ (dotted line), $\rho = 0.4$ (short-dashed line), $\rho = 0.6$ (long-dashed line), and $\rho = 0.8$ (solid line). The ratio between the lattice constant and the outer diameter of the cylinders is taken to be $x = 1.5$.

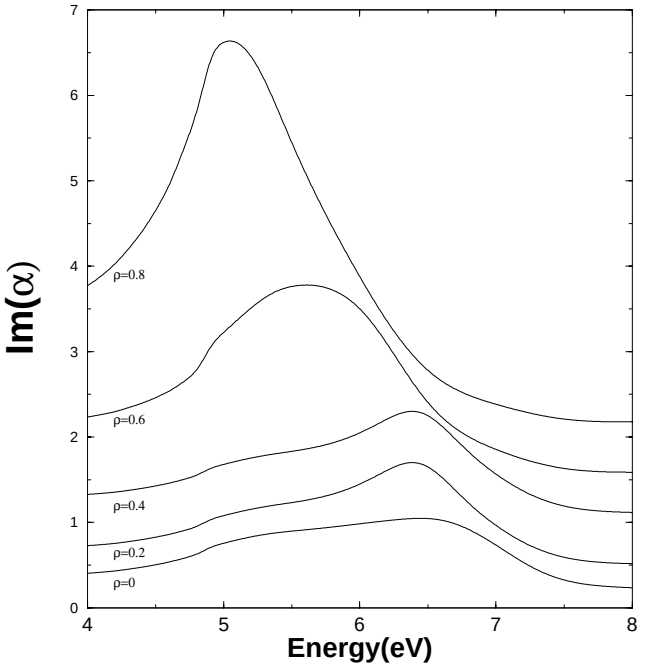

Fig. 7. Same as Figure 3, as obtained from equation (8) with use of the actual principal dielectric functions $\varepsilon_\perp(\omega)$ and $\varepsilon_\parallel(\omega)$ of graphite.

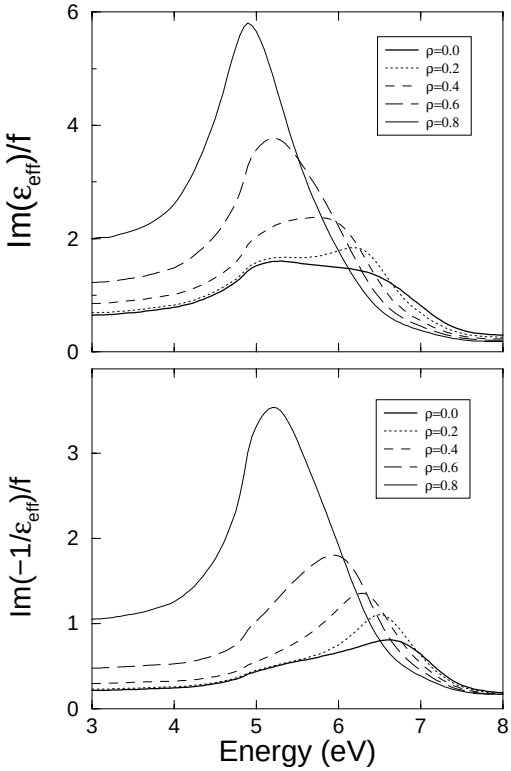

Fig. 8. Same as Figure 6, as obtained from equations (6) and (7) with use of the actual principal dielectric functions $\varepsilon_\perp(\omega)$ and $\varepsilon_\parallel(\omega)$ of graphite.

equations (17) and (18), have been represented for $x = 1.5$ and various values of ρ. We also note that as x decreases the low-energy ($u = m_-$) and high-energy ($u = n_+$) modes, whose energy position depends only weakly on ρ, dominate the optical absorption and energy-loss, respectively.

The role of anisotropy is displayed in Figures 7 and 8. In these figures, we have plotted $\mathrm{Im}\,\alpha(\omega)$ (Fig. 7), $\mathrm{Im}\,\varepsilon_{\mathrm{eff}}(\omega)/f$ (Fig. 8), and $\mathrm{Im}[-\varepsilon_{\mathrm{eff}}^{-1}(\omega)]/f$ (Fig. 8), as obtained from equations (8), (6) and (7) with full inclusion of the anisotropic dielectric function of graphite and for various values of ρ, as in Figures 3 and 6. With the presence of anisotropy, the two-mode structure exhibited by equations (11) , (17) and (18) is replaced by a more complicated spectral representation. One sees from Figure 7 that the tangential plasmon peak-position of isolated cylinders remains fairly insensitive to the anisotropy of carbon nanotubes. However, its shape drastically changes, as a consequence of the presence of a nearly constant and positive dielectric function $\varepsilon_\parallel$, and the radial resonance condition is not visible. For $x = 3$ the MG dielectric function is found to nearly coincide with the isolated-cylinder result, as in the isotropic case. As the distance between the cylinders decreases, the impact of the anisotropy is still to soften the resonances. Furthermore, one sees from Figure 8 that now at small values of ρ the low-energy resonance is only visible in the optical absorption, while the energy loss only exhibits the high-energy peak.

3.1.1 Packed regime

In this section we present results of our calculation of the effective dielectric function of a periodic array of carbon nanotubes, as obtained from equation (10) with full inclusion of both the anisotropy and the electromagnetic interaction between the tubules. All calculations presented here have been found to be insensitive to the precise value of the number of mesh points in the unit cell. For metallic structures, sampling meshes as large as 180×180 have been found to be required to provide well-converged results [19]; however, for carbon nanotubes sampling meshes of 60×60 have been found to provide well-converged results, which is due to the smoothing effect of the large damping originated with the presence of interband transitions in graphite.

In Figures 9 and 10 we show our full calculations of the p component of the effective dielectric function of an array of plain ($\rho = 0$) carbon nanotubes, as obtained for various values of the ratio x between the lattice constant and the outer diameter of the cylinders: $x = 2.0$, $x = 1.5$ and $x = 1.3$ in Figure 9, and $x = 1.1$ and $x = 1.03$ in Figure 10. Also plotted in these figures by dotted lines are calculations of the MG dielectric function of equations (6) and (7). These calculations show that the actual effective dielectric function is well described by the MG approximation in the low-filling-ratio regime, our full calculations beginning to deviate from those obtained within the MG approximation at $x \sim 1.3$. For smaller concentrations of graphite, multipolar modes cannot be neglected and the dipole-resonance positions necessarily deviate, as discussed in reference [19].

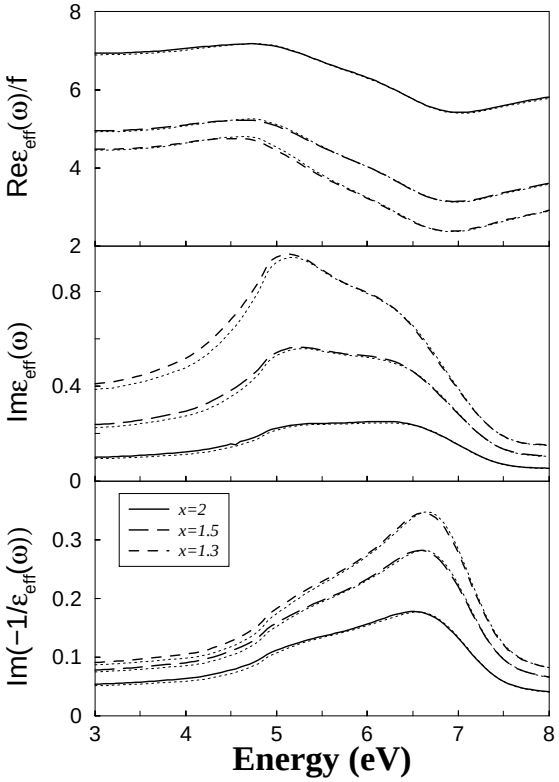

Fig. 9. The real and imaginary parts of the long-wavelength effective dielectric function, $\mathrm{Re}\,\varepsilon_{\rm eff}(\omega)$ and $\mathrm{Im}\,\varepsilon_{\rm eff}(\omega)$, and the energy-loss function, $\mathrm{Im}[-\varepsilon_{\rm eff}^{-1}(\omega)]$, of a periodic array of plain ($\rho = 0$) carbon nanotubes, for p polarized electromagnetic excitations. Solid, long-dashed, and short-dashed lines represent our full calculated results, as obtained from equation (10) for ratios between the lattice constant and the outer diameter of the cylinders $x = 2$, $x = 1.5$, and $x = 1.3$, respectively. The dotted lines represent MG results, as obtained from equations (6) and (7).

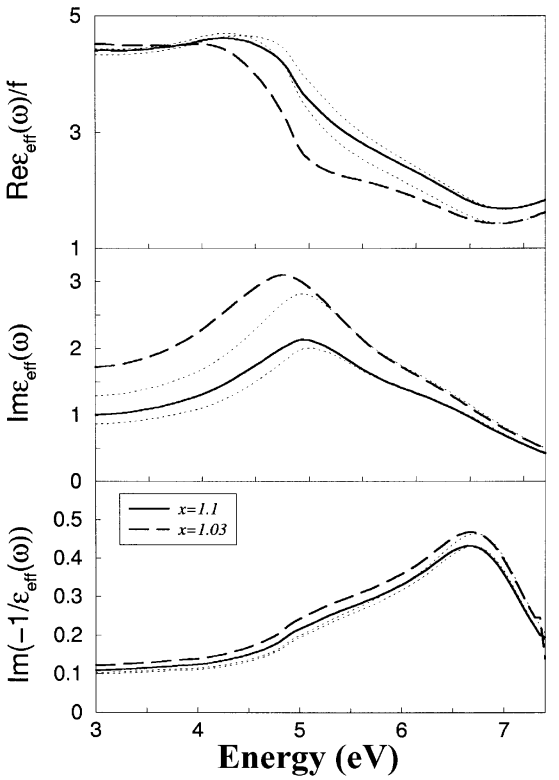

Fig. 10. Same as Figure 9, for ratios between the lattice constant and the outer diameter of the cylinders $x = 1.1$ (solid line) and $x = 1.03$ (dashed line).

One sees from Figures 9 and 10 that, as within the MG approach, the trend with increasing the concentration of tubules is for the actual dipolar peak in $\mathrm{Im}\,\varepsilon_{\rm eff}(\omega)$ and $\mathrm{Im}[-\varepsilon_{\rm eff}^{-1}(\omega)]$ to be shifted from the isolated-cylinder dipole mode at ~ 6.5 eV to lower and higher energies, respectively. When the nanoparticles are brought into close contact, electromagnetic coupling between them converts the dipolar surface mode into a very localized one, trapped in the region between the nanostructures, and the MG approximation fails to describe the details of the effective dielectric function. We note that multipolar resonances, which are present in the close-contact regime, are not visible in the spectra due to the smoothing effect of the large damping characteristic of graphite. At higher concentrations of tubules, when graphite forms a connected medium ($x \leq 1$), dipolar modes cannot be excited. Hence, optical absorption exhibits a single peak originated in the maximum of $\mathrm{Im}\,\varepsilon(\omega)$ at ~ 4.6 eV, and the energy-loss function shows a single peak at the bulk plasmon resonance at ~ 7 eV. Besides these peaks, there is a background of unresolved multipole contributions to $\mathrm{Im}\,\varepsilon_{\rm eff}(\omega)$ and $\mathrm{Im}[-\varepsilon_{\rm eff}^{-1}(\omega)]$ in the plasmon region with energies between ~ 5 and ~ 7 eV.

Calculations of the p component (p polarization) of the effective dielectric function of a periodic array of hollow ($\rho \neq 0$) carbon nanotubes were reported in reference [15] for various ratios ρ between inner and outer radii of the tubules. As in the case of plain cylinders ($\rho = 0$), these calculations nearly coincide for $x = 2.0$ with the results obtained within the MG approximation. However, in the close-packed regime ($x = 1.03$) the strong electromagnetic coupling between the tubes results in non-negligible contributions from multipolar resonances. This multipolar coupling provokes a redshift and a blueshift of the MG dipolar resonances that are visible in the optical spectra and the energy loss, *i.e.*, the low-energy ($u < 1/2$) dipolar mode with tangential symmetry and the high-energy ($u > 1/2$) dipolar mode with radial symmetry. A comparison between these calculations and the experimentally determined macroscopic p dielectric function of close-packed carbon nanotubes [12] was also presented in reference [15], showing an excellent agreement for $\rho = 0.6$, which yields in the close-packed regime ($x = 1.03$) a filling fraction $f \sim 0.5$.

Finally, we look at the **E**-field pattern associated with the electromagnetic resonances that are present in the optical absorption and the energy loss. In Figure 11, we show detailed pictures of the intensity of the electric field and the corresponding charge density generated by normally incident p-polarized light impinging on our periodic array of hollow ($\rho = 0.6$) carbon nanotubes with $x = 2$.

The frequency of the incident radiation has been chosen to be $\omega_1 = 5.2$ eV and $\omega_2 = 5.9$ eV, corresponding to

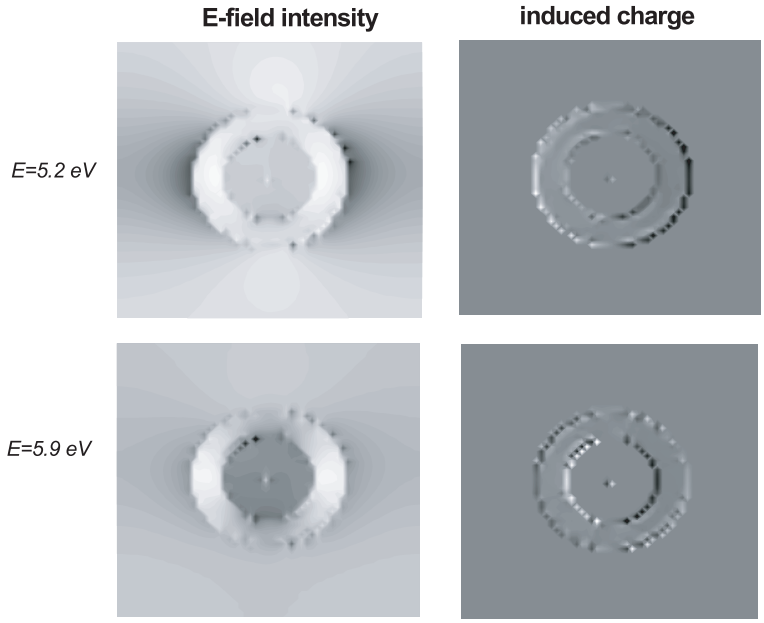

Fig. 11. The intensity of the electric field and the corresponding charge density generated by a normally incident p polarized electromagnetic plane wave impinging on a periodic system of hollow ($\rho = 0.6$) carbon nanotubes with $x = 2.0$. Both the electric field and the induced charge have been evaluated at two different frequencies: $\omega_1 = 5.2$ eV (the frequency at which the optical absorption is maximum) and $\omega_2 = 5.9$ eV (the frequency at which the energy loss is maximum). White/dark areas mean small/large values of the electric-field intensity and the induced charge.

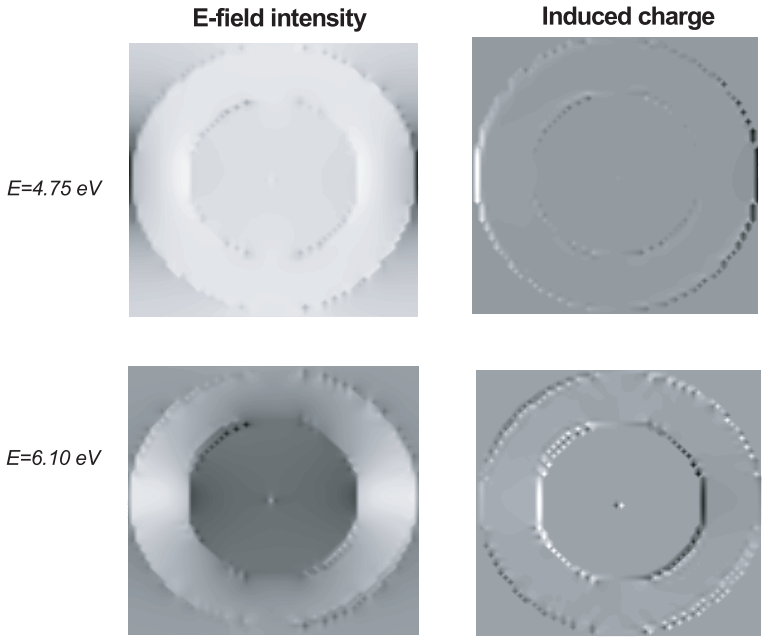

Fig. 12. Same as Figure 11, for $x = 1.03$, $\omega_1 = 4.75$ eV, and $\omega_2 = 6.1$ eV.

the location of resonances in the optical absorption and the energy loss, respectively. In this figure one clearly sees that the incident radiation is exciting prototypical dipolar tangential and radial dipolar plasmons at the surfaces of a nearly isolated hollow cylinder. At $\omega_1 = 5.2$ eV, the intensity of the electric field is maximum outside the nanotube and the induced charge is clearly located on the outer surface of the tubule, showing a tangential field pattern. At $\omega_2 = 5.9$ eV, the **E**-field intensity is maximum in the hollow core of the nanotube and the induced charge is located on both surfaces of each tubule, though the largest part of it is located on the inner surface of the tube. These represent the main characteristics of a radial dipolar mode.

In the case of a close-packed structure, the incident radiation excites a very localized tangential surface plasmon. This is illustrated in Figure 12, where we show pictures of the **E**-field intensity and the corresponding charge density generated by normally incident p-polarized light

impinging on our periodic array of hollow ($\rho = 0.6$) carbon nanotubes with $x = 1.03$. At $\omega_1 = 4.75$ eV, where the optical absorption exhibits a maximum, the **E**-field intensity is strongly enhanced in the region between the tubes and the induced charge is clearly localized, showing a strongly localized tangential field pattern. At $\omega_2 = 6.1$ eV, where the energy loss is maximum, one clearly sees that the incident radiation is exciting a radial surface plasmon which is very similar to that observed in the case of nearly isolated nanotubes (see Fig. 11).

4 Summary and conclusions

We have reported extensive calculations of the effective electronic response of aligned multishell carbon nanotubes, of interest in the interpretation of absorption spectra and electron energy-loss experiments. A local graphite-like dielectric tensor has been assigned to every point of the multishell tubules, and the effective dielectric function of the composite has been computed by solving Maxwell's equations in media with tensor-like dielectric functions. A MG-like approach appropriate to the case of infinitely long anisotropic tubules has also been developed, showing that MG results are accurate as long as the distance between the axis of neighboring plain tubules is not smaller than ~ 1.3 times the outer diameter of the cylinders.

The effective response of carbon nanotubes has been found to be sensitive to both the inner cavity of hollow tubules and the anisotropy, which we have first investigated with use of the MG approximation. Within this approach, we have analyzed the mode strengths and positions of tangential and radial surface plasmons, and have investigated the effect of the anisotropy and the electromagnetic interactions between the tubes.

Finally, we have presented an analysis of the electric-field pattern associated with the electromagnetic resonances that are present in the optical absorption and the energy loss. We have shown that incident p-polarized light impinging on a periodic array of hollow carbon nanotubes excites tangential and radial plasmons at the surfaces of each tubule. In the case of isolated hollow nanotubes, these surface plasmons are found to be prototypical dipolar modes. In the close-packed regime, where nanotubes are nearly touching, our calculations indicate that the incident radiation excites a very localized tangential surface plasmon, while the radial plasmon is found to be very similar to that observed in the case of isolated nanotubes.

J. M. P. gratefully acknowledges partial support by the University of the Basque Country, the Basque Hezkuntza, Unibertsitate eta Ikerketa Saila, and the Spanish Ministerio de Educación y Cultura.

References

1. S. Iijima, Nature **354**, 56 (1991).
2. T.W. Ebbesen, P.M. Ajayan, Nature **358**, 220 (1992); P.M. Ajayan, T.W. Ebbesen, Rep. Prog. Phys. **60**, 1025 (1997).
3. M.F. Lin, K.W.K Shung, Phys. Rev. B **47**, 6617 (1993).
4. O. Sato, Y. Tanaka, M. Kobayashi, A. Asegawa, Phys. Rev. B **48**, 1947 (1993).
5. P. Longe, S.M. Bose, Phys. Rev. B **48**, 18239 (1993).
6. R. Kuzuo, M. Terauchi, M. Tanaka, Jpn J. Appl. Phys. **31**, L1484 (1992).
7. P.M. Ajayan, S. Iijima, T. Ichihashi, Phys. Rev. B **47**, 6859 (1993).
8. L.A. Bursill, P.A. Stadelmann, J.L. Peng, S. Prawer, Phys. Rev. B **49**, 2882 (1994).
9. T. Stöckli, J.M. Bonard, P.A. Stadelmann, A. Chatelain, Z. Phys. D **40**, 425 (1997).
10. O. Stephan, P.M. Ajayan, C. Colliex, F. Cyrot-Lackmann, E. Sandre, Phys. Rev. B **53**, 13824 (1996).
11. P.M. Ajayan, O. Stephan, C. Colliex, D. Trauth, Science **265**, 1212 (1994).
12. W.A. de Heer, W.S. Bacsa, A. Chatelain, T. Gerfin, R. Humphrey-Baker, L. Forro, D. Ugarte, Science **268**, 845 (1995).
13. F. Bommeli, L. Degiorgi, P. Wachter, W.S. Bacsa, W.A. de Heer, L. Forro, Solid. State. Commun. **99**, 513 (1996).
14. F.J. García-Vidal, J.M. Pitarke, J.B. Pendry, Phys. Rev. Lett. **78**, 4289 (1997).
15. J.M. Pitarke, F.J. García-Vidal, Phys. Rev. B **63**, 73404 (2001).
16. J.C. Maxwell-Garnett, Philos. Trans. R. Soc. London A **203**, 385 (1904); **205**, 237 (1906); see, also, C.F. Bohren, D.R. Huffman, *Absorption and Scattering of light by Small Particles* (Wiley, New York, 1983).
17. A.A. Lucas, L. Henrad, Ph. Lambin, Phys. Rev. **49**, 2888 (1994).
18. J.M. Pitarke, J.B. Pendry, P.M. Echenique, Phys. Rev. B **55**, 9550 (1997); J.M. Pitarke, A. Rivacoba, Surf. Sci. **377**, 294 (1997).
19. J.M. Pitarke, F.J. García-Vidal, J.B. Pendry, Phys. Rev. B **57**, 15261 (1998).
20. D.J. Bergman, D. Stroud, Solid State Phys. **46**, 147 (1992).
21. J.M. Pitarke, F.J. García-Vidal, J.B. Pendry, Surf. Sci. **433**, 605 (1999).
22. L. Henrad, Ph. Lambin, J. Phys. B **29**, 5127 (1996).
23. J.B. Pendry, A. MacKinnon, Phys. Rev. Lett. **69**, 2772 (1992); J.B. Pendry, J. Mod. Opt. **41**, 2417 (1994).
24. A.J. Ward, J.B. Pendry, J. Mod. Opt. **43**, 773 (1996).
25. *Handbook of Optical Constants of Solids*, edited by E.D. Palik (Academic, New York, 1985).
26. E.A. Taft, H.R. Philipp, Phys. Rev. **138**, A197 (1965).
27. R.H. Ritchie, Phys. Rev. **106**, 874 (1957).
28. A.A. Lucas, L. Henrad, Ph. Lambin, Nucl. Instrum. Methods B **96**, 470 (1995).